Monthly Notices of the ROYAL ASTRONOMICAL SOCIETY

MNRAS **537,** 2334–2341 (2025) https://doi.org/10.1093/mnras/stae2643
Advance Access publication 2024 November 26

# Simultaneous two-colour intensity interferometry with H.E.S.S.

Naomi Vogel,* Andreas Zmija, Frederik Wohlleben ,† Gisela Anton, Alison Mitchell ,
Adrian Zink and Stefan Funk

*Erlangen Centre for Astroparticle Physics, Friedrich-Alexander-Universität Erlangen-Nürnberg, Nikolaus-Fiebiger-Str. 2, Erlangen 91058, Germany*

Accepted 2024 November 20. Received 2024 November 11; in original form 2024 September 2

## ABSTRACT

In recent years, intensity interferometry has been successfully applied to the Imaging Atmospheric Cherenkov Telescopes, H.E.S.S. , MAGIC, and VERITAS. All three telescope systems have proven the feasibility and capability of this method. After our first campaign in 2022, when two of the H.E.S.S. telescopes in Namibia were equipped with our external set-up and the angular diameter of two stars was measured, our set-up was upgraded for a second campaign in 2023, where the goal is to perform simultaneous two-colour measurements. The second campaign not only involves a third equipped telescope, but also each mechanical set-up now includes two interference filters at two different wavelengths (375 and 470 nm) with a broader bandwidth of 10 nm. This enables having simultaneous two-colour measurements, which yield information about the star's physical size at different wavelengths. This is the first time that simultaneous dual-waveband intensity interferometry measurements have been performed. We report the angular diameter results of four stars, Mimosa ($\beta$ Cru), Eta Centauri ($\eta$ Cen), Nunki ($\sigma$ Sgr), and Dschubba ($\delta$ Sco), where the effects of limb darkening are also taken into account.

**Key words:** instrumentation: high angular resolution – instrumentation: interferometers – methods: observational – techniques: interferometric – telescopes – stars: imaging.

## 1 INTRODUCTION

Intensity interferometry was first employed in the 1960s by Robert Hanbury Brown and Richard Q. Twiss (hereafter, HBT), resulting in a successful operation of the Narrabri Stellar Intensity Interferometer (NSII) that measured the angular diameter of 32 stars (Hanbury Brown, Davis & Allen 1967, 1974). As the development of fast electronics and large area collectors was lagging behind, the technique was discarded in the field of astronomy to make way for stellar amplitude interferometry, which has developed into notable interferometric instrumentation at, for example, the Center for High Angular Resolution Astronomy (CHARA; ten Brummelaar et al. 2005) and the Very Large Telescope Interferometer (VLTI; Haguenauer et al. 2010). The technique exploits the first-order coherence of electromagnetic waves from a source observed by separated telescopes, connecting the phases and amplitudes. As a result of atmospheric turbulence, the baselines between the telescopes are limited and thus the optical resolution is limited to some 0.1 mas. In contrast to amplitude interferometry, intensity interferometry exploits the second-order correlation, the square of the wave amplitude relating to its intensity, making it essentially unresponsive to either the telescope's optical deficiencies or to atmospheric turbulence. The possibility of kilometre-long baselines in the optical wavelength range raises the concept of microarcsecond imaging (Dravins 2016).

Therefore, intensity interferometry has gained additional astronomical interest in the last two decades and efforts have been made to implement it using the Imaging Atmospheric Cherenkov Telescopes (IACTs), which are ground-based gamma-ray telescopes. Their advantages are the large diameters (>10 m) and the array-like layout, not only allowing for baselines of the order of 100 m (LeBohec & Holder 2006) up to 2 km but also offering many different baselines at the same time in the case of the future Cherenkov Telescope Array Observatory (CTAO; Dravins et al. 2013).

The IACT observatories, H.E.S.S., MAGIC, and VERITAS, have already successfully demonstrated the efficiency of realizing stellar intensity interferometry (SII) measurements. The VERITAS-SII measured the diameters of two B stars ($\beta$ CMa and $\varepsilon$ Ori) with all its four telescopes (Abeysekara et al. 2020) and is extending their measurements to stars of higher magnitude and making further improvements concerning the angular resolution (Kieda 2022). A recent publication is about their angular diameter measurements of the star $\beta$ UMa (Acharyya et al. 2024) at visual wavelengths (416 nm), which are consistent with the results of CHARA measurements in the infrared region. MAGIC started out by measuring the correlation signal at different telescope baselines of three stars: $\varepsilon$ CMa (Adhara), $\eta$ UMa (Benetnasch), and $\beta$ CMa (Mirzam) (Acciari et al. 2020). Their active mirror control allows for subtelescope baselines and zero-baseline correlation measurements. An improved sensitivity is expected by adding the CTA LST-1 to the interferometer (Cortina et al. 2022). Abe et al. (2024) recently published measurements of 22 stellar diameters.

In 2022 April, the first intensity interferometry measurements were conducted with the H.E.S.S. telescopes in Namibia by mounting intensity interferometry set-ups to the lid of the camera of two

* E-mail: naomi.vogel@fau.de
† Present address: Max-Planck_Institution für Kernphysik, Saupfercheckweg 1, Heidelberg 69117, Germany

telescopes. Two single stars in the Southern hemisphere, Shaula ($\lambda$ Sco) and Nunki ($\sigma$ Sgr), were successfully observed. Due to the installation of a beamsplitter in the optics of each telescope, zero-baseline correlations were possible (Zmija et al. 2023).

After having proven that the approach of intensity interferometry works with the H.E.S.S. telescopes, our team considered alternative concepts for interferometric application, starting with simultaneous two-colour intensity interferometry measurements. This paper presents our second intensity interferometry campaign in 2023 April/May at the H.E.S.S. telescopes where we not only integrated a third telescope into our interferometer, but also expanded our optical set-up to two different colour filters (375 and 470 nm). This is the first time that intensity interferometry measurements were performed simultaneously in two different wavebands at an IACT. It also represents the shortest wavelength that has been employed thus far for intensity interferometry observations. Three single stars in the Southern hemisphere were observed and also studied by HBT: Mimosa ($\beta$ Cru), Eta Centauri ($\eta$ Cen), and Dschubba ($\delta$ Sco) (Hanbury Brown, Davis & Allen 1974). In addition, we repeated measurements on $\sigma$ Sgr ($\sigma$ Sgr) for comparison with two colours, as well as reducing statistical uncertainties despite having less observation time (see Section 6.2). In summary, this demonstrates that multiwaveband intensity interferometry measurements are feasible and could provide the potential to enhance signal-to-noise in future intensity interferometry observations.

Hereafter, we first review the physical quantities of SII in Section 2. The differences of the experimental set-up with its new application are described in Section 3. In Section 4, we briefly revisit our measurement procedure and in Section 5 we outline the details of our analysis for the recorded data. Section 6 gathers the final angular diameters of our target stars.

## 2 THEORETICAL REVIEW

Here we provide a short theoretical review; see Hanbury Brown (1974) for further information.

The projected distance between two telescopes as seen from a given star is the so-called projected baseline $r$, which changes when the star moves across the sky. An intensity interferometer correlates the intensity signals $I_1$ and $I_2$ recorded at each telescope as a function of the projected baseline, resulting in the second-order correlation function,

$$g^{(2)}(r,\tau) = \frac{\langle I_1(0,t) I_2(r,t+\tau)\rangle}{\langle I_1\rangle\langle I_2\rangle}, \tag{1}$$

where $\tau$ is an applied time shift between the two signals and $\langle\,\rangle$ is the average over time $t$.

The Siegert relation (Siegert 1943; Ferreira et al. 2020) connects the second-order correlation function to the first-order correlation function by

$$g^{(2)}(r,\tau) = 1 + |g^{(1)}(r,\tau)|^2, \tag{2}$$

and the first-order correlation can also be separated into a spatial and temporal part,

$$g^{(1)}(r,\tau) = g^{(1)}(r) g^{(1)}(\tau). \tag{3}$$

The spatial component, also referred to as visibility, is expressed by the Fourier transform of the source's spatial intensity distribution, which is described by the van Cittert–Zernike theorem (Mandel & Wolf 1995). Especially for a star that is considered as a disc of uniform intensity up to an angular diameter $\theta$, the first-order correlation is given by

$$g^{(1)}(r) = 2\frac{J_1(\pi r\theta/\lambda)}{\pi r\theta/\lambda}, \tag{4}$$

where $J_1$ is the Bessel function of first kind and $\lambda$ is the wavelength of light. The second-order correlation $g^{(2)}(r) - 1 = |g^{(1)}(r)|^2$, observed in an intensity interferometer, is referred to as squared visibility. The so-called resolving baseline is identified by the first zero at $r \approx 1.22\lambda/\theta$ and increases for smaller sources or larger wavelengths. Measuring the squared visibility over a broad range of baselines (squared visibility curves) allows us to determine the angular size of the star.

The temporal component in equation (3) is expressed by the Fourier transform of the light spectral density, which is described by the Wiener–Khinchin theorem (Mandel & Wolf 1995). In a measurement of $g^{(2)}(\tau)$, a photon bunching peak should be visible in the temporal range of the coherence time,

$$\tau_c := \frac{\lambda_0^2}{c\Delta\lambda}, \tag{5}$$

where $c$ is the speed of light, $\lambda_0$ is the central wavelength, and $\Delta\lambda$ is the optical bandwidth. When using optical filters with a bandwidth of the order $\Delta\lambda = 1$ nm, the coherence time is of the order of 1 ps, which is much shorter than what can be resolved by detector systems. Instead, only the integral under $g^{(2)}(r) - 1$ can be measured. As the value of the coherence time decreases to broader bandwidths, but photon rates and thus photon statistics increase, the signal-to-noise of a measurement is independent of the used optical bandwidth.

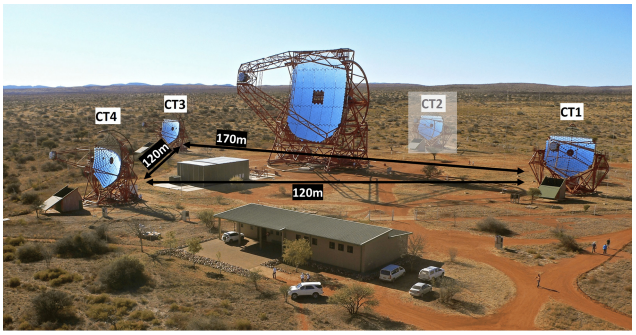


**Figure 1.** The H.E.S.S. site. In 2002, the Phase I telescopes (CT1–CT4) were inaugurated. The central telescope was built in 2012. In 2023, the intensity interferometry set-ups were mounted on telescopes CT1, CT3, and CT4. The control building (bottom centre) is used to operate the telescopes and for part of the data analysis.

## 3 THE SII SYSTEM AT H.E.S.S.

### 3.1 The H.E.S.S. telescopes

For the intensity interferometry campaign in 2023, three of the H.E.S.S. telescopes (Phase I) were used, which are situated in the Khomas Highlands in Namibia at an altitude of 1835 m above sea level. Four IACTs make up a square with 120 m side length and 170 m diagonal length, with a 600 m$^2$ mirror area telescope at its centre, which was added in 2012 (see Fig. 1). The mirror area of a phase I telescope is compromised of 382 round mirror facets leading to a total area of 108 m$^2$, a diameter of 12 m and a focal length of 15 m. The telescopes are built according to the Davis–Cotton design.[1]

[1]See https://www.mpi-hd.mpg.de/HESS/pages/about/telescopes/.

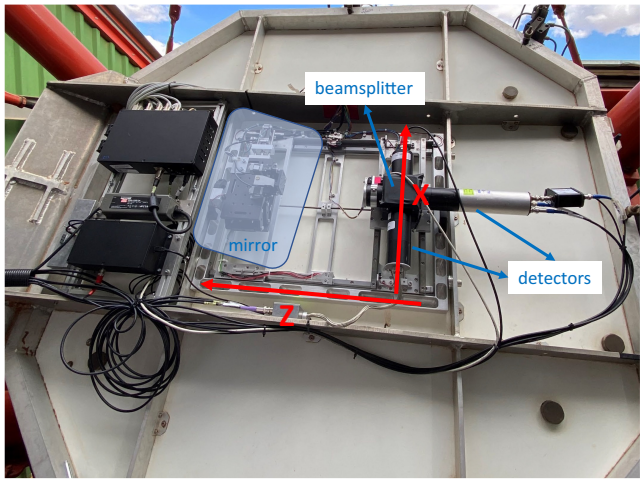


**Figure 2.** Intensity interferometry set-up mounted to the lid of the telescope CT3. The mirror was not installed when the picture was taken. Its position is indicated by the blue shaded area on the left side of the set-up. The red arrows mark the range of motion for each individual component, which is equipped with motors.

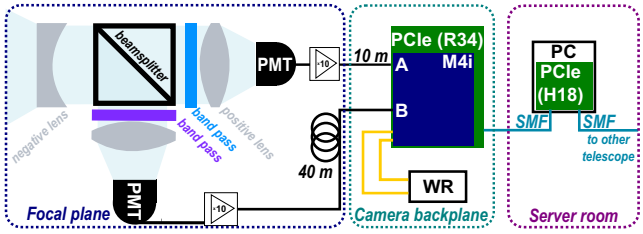


**Figure 3.** Schematic diagram of the intensity interferometer including optics and data transfer. Each telescope has an identical set-up. The bandpass filter for the transmitted light has a wavelength of 470 nm and the one for the reflected beam a wavelength of 375 nm. Both have a bandwidth of 10 nm. The main difference to the optics of the 2022 campaign is the order of lenses and filters. For the single colour measurements in 2022, the order was lens–filter–lens–beamsplitter–detectors. For the two waveband measurements in 2023, the order was lens–beamsplitter–filters–lens–detectors.

The main goal for intensity interferometry is a submilliarcsecond resolution, which is reached by relating large light collecting areas and long telescope baselines. These requirements make the H.E.S.S. telescopes suitable candidates.

### 3.2 Experimental set-up

The intensity interferometry set-up was designed to fit on the lid of the H.E.S.S. Phase I cameras. Fig. 2 shows the set-up mounted in the centre of the camera lid in the focal spot of the H.E.S.S. mirrors. The set-up is described in Zmija et al. (2023). A third set-up was constructed according to this design. The rectangular base $50 \times 63\,\mathrm{cm}^2$ is made of aluminium with a total weight of 21 kg including all attached equipment. Fig. 3 shows a schematic diagram of the set-up. The 45° angled mirror reflects the incoming light beam (from the left side) into the optical system and on to the two detectors.

The mirror for the additional third telescope is also a SEA-VIS front-surface mirror produced via CNC, precision-cut by Präzisions Glas & Optik GmbH, and is glued to an aluminium frame for stabilization.

As the measurements for the 2023 campaign are done with two colour filters simultaneously (see Fig. 3) the optics within the optical path are arranged differently than for the previous one-colour measurements. The light beam first encounters a parallelizing lens (coated concave lens, $F = -75$ mm) in a 2-inch tube system and is then split into two beams by a dichroic beamsplitter plate with a cut-on wavelength at 415 nm. The transmitted beam is lead through a LC-HBP470/10-50 narrow-band optical (interference) filter [470 nm central wavelength (CWL), 10 nm width] and the reflected beam through a LC-HBP375/10-50 narrow-band optical (interference) filter (375 nm CWL, 10 nm width). Both beams are then focused on to the active area of the photomultiplier tube (PMT) using a converging lens (coated bi convex lens, $F = 100$ mm). The lenses are manufactured by Thorlabs, Inc.,[23] the beamsplitter and the interference filter by Laser Components, Inc.[4] We decided to increase the bandwidth of the interference filters from 2 to 10 nm after successful laboratory experiments with broader optical bandwidths. We confirmed that we are able to control higher photon rates than the ones we had in the 2022 campaign and also to measure smaller correlation peaks. The reason for the increase in bandwidth is to decrease systematic errors in the measurements. In particular, the aim is to decrease the uncertainty on the actual effective filter bandwidth, which comes from light beams hitting the interference filters at non-perpendicular inclinations, which are always present due to imperfect parallelization of the collimated beam. Because we use two interference filters with different CWLs, we decided to also use two different photomultiplier types manufactured by Hamamatsu for optimal performance.[5] For the filter with 470 nm, we use the PMT R11265U-300 with a peak sensitivity at 420 nm and a quantum efficiency of 39 per cent. It has a quantum efficiency of 30 per cent at the relevant wavelength of 470 nm and was also used in our campaign in 2022. For the filter with 375 nm, we use the PMT R11265U-200 with a peak sensitivity at 400 nm and a quantum efficiency of 43 per cent, also at 375 nm. The high voltage (HV) power supply is placed in the camera backplane and supplies the first nine dynodes. To stabilize the voltage at high rates, the last four dynodes are powered by a further booster power supply. The amplifier is situated directly behind the PMT on the right side (transmitted beam) and on the bottom of the set-up for the lower PMT (reflected beam) to reduce electronic noise (see Fig. 2). The amplified PMT signals are transported through airborne five low-loss, double shielded coaxial cables with 10 and 40 m length to evade any crosstalk at the sampling interface.

To counteract any inevitable mis-pointing of the telescopes, which for H.E.S.S. operation is not online-corrected, each item of the set-up is assembled with stepper motors, which can be moved remotely, to ensure that a maximum amount of the light beam is captured by the optical system. The mis-pointing is fn the order of $<1$ cm to 5 cm depending on the elevation. The red arrows in Fig. 2 demonstrate the range of motion for the different items of the system. The optics and detectors can be moved in the camera plane ($x$- and $z$-axis) and the mirror in $z$-axis and $y$-axis (up and down). The motors rotating the mirror around the $x$- and $z$-axis were removed as they did not show any sufficient improvement in bringing the spot more into focus during the campaign in 2022. The motor control box and its power

[2]See https://en.wikipedia.org/wiki/High_Energy_Stereoscopic_System.
[3]See https://www.thorlabs.com/navigation.cfm?guide_id=2264.
[4]See https://www.lasercomponents.com/de/produkt/standard-bandpassfilter/.
[5]For details, see https://www.hamamatsu.com/content/dam/hamamatsu-photonics/sites/documents/99_SALES_LIBRARY/etd/R11265U_H11934_TPMH1336E.pdf.

supply are positioned to the left of the set-up on the lid. Both HV cables and signal cables are brought to the camera backplane where the HV power supply and the digitizer are installed.

Besides the HV power supply, a M4i.2211-×8 digitizer from Spectrum Instrumentation[6] is installed in two of the telescopes' backplane racks, as described in Zmija et al. (2023). The four channel version of this digitizer is installed in the third telescope, although we only use two of them for the two PMTs. After the PMT currents are transformed to voltages, which are proportional to the currents, they are sampled by the digitizers at a speed of 625 MS $s^{-1}$ at a digitization range of ±200 mV. Using the R34 PCIe board system from Adnacom,[7] the PCIe bus of the workstation is extended to each telescope via optical fibre.

It is important that all three data streams are synchronized. This is ensured by connecting each digitizer to the White Rabbit (WR) network of the H.E.S.S. telescopes. The pulse per second (PPS) of the WR triggers the digitizers and they sample 2 GS of data synchronously, which amounts to 3.436 s of data taking. The next sampling starts with the PPS 4 s after the previous triggered sampling and the process is repeated. The duty cycle of the procedure is 85.9 per cent. A 10-MHz clock is used as reference to generate a synchronized sampling timebase for all three telescope digitizers.

During the measurements, the data are stored on hard disks to be correlated offline during the day or after the campaign.

## 4 MEASUREMENT PROCEDURE

As gamma ray observations do not take place during the H.E.S.S. moonlight break – when the Moon has a fraction of lunar illumination of 0.6 and is above the horizon – we can make use of that time for our intensity interferometry observations, which were carried out in 2023 April/May. This campaign's main targets of observations are the stars, $\beta$ Cru, $\eta$ Cen, $\delta$ Sco, and, for comparison to the campaign of 2022, $\sigma$ Sgr. They were selected taking into account their configuration, trajectory, magnitude, and separation to the Moon. All results are presented in Section 6.

The procedure of our measurements is identical to that of the 2022 campaign described in Zmija et al. (2023). At the beginning of our measurement time for one night, the three telescopes are positioned on one of the chosen stars and start tracking it until targets are changed (when the star is less than $\approx 30^\circ$ above the horizon) or the night is over (when the Sun is only $10^\circ$ below the horizon). The second step is to perform a PMT calibration with the HV turned off in order to extract the direct current (DC) offset in the analysis later on. Then a PMT pulse calibration with the HV turned on is carried out to establish the live photon rates by using the shape and height distribution of the photon pulses. The incoming photon rates have to be low for calibration, which we accomplished by moving our motor system so our optics are just out of focus of the star. Details of the calibration can be found in Zmija et al. (2021).

To focus the optics directly on the star, we perform our online pointing correction by adjusting the individual parts of the set-up with the motors to achieve maximal photon rates. When the optimal photon rate is found, the data taking begins. Due to mis-pointing of the telescopes it happens that over time during the observations the optical system is no longer in the focus of the star beam (as noticed via a drop in photon rate) and the optical elements are adjusted via moving the motors. When the measurements end the HV is shut down and the motors are moved to their parking position. The telescopes are parked, the amplifiers turned off and the correlation analysis of the acquired data starts.

## 5 DATA ANALYSIS

### 5.1 Correlation procedure and data corrections

The temporal correlation of the PMT currents (waveforms) is performed after the measurements are taken. As we use three telescopes (CT1, CT3, and CT4), each with two colours (channel A and B; see Section 3), there are three binary files, each including the two channels A and B. Using the correlation function from the Python package *cupy*, the six waveform channels are first read from the hard disk and then correlated. For each colour channel, there are three possible telescope combinations (1–3, 1–4, and 3–4). Due to a malfunctioning amplifier, not all three telescopes were in operation simultaneously the whole time but only two at a time. Therefore, the stars $\beta$ Cru and $\eta$ Cen only show the combinations 1–4 and 3–4 in later analysis results. At the end of the campaign, all three telescopes were running simultaneously, as seen in the $\sigma$ Sgr and $\delta$ Sco results.

Before further analysis is done, the correlated data are cleaned by adding a lowpass filter with a cut-off frequency of 200 MHz and notch filters to remove sharp noise frequencies. Furthermore, the optical path delay correction is applied to correct for the difference of the optical path-length at the different telescopes. More detailed information about the noise cuts and the optical path delay correction can be found in Zmija et al. (2023). Because only channels with similar cable lengths between the telescopes – for example, CT1 channel A with CT4 channel A (both $\approx 10$ m cable length) or CT1 channel B with CT4 channel B (both $\approx 40$ m cable length) – are correlated, no cable delay correction has to be applied.

### 5.2 Data preparation and signal extraction

After the data corrections are applied, the data of each star are bundled into time segments to track the change in squared visibility and to determine the angular size of the star. For each segment, the temporal $g^{(2)}$ function is calculated by normalization of the correlated data. However, when splitting the data into segments, it becomes apparent that the photon-bunching peak is not always significantly detected, especially at large baselines. This complicates fitting a Gaussian function to the signal peak to extract the squared visibility. To stabilize the fit in each segment, global Gaussian fit parameters are extracted. Therefore, the data of all stars for each telescope combination are collected and averaged, with each data array weighted by the inverse square of the standard error (rms) of the noise of the $g^{(2)}$ function in order to account for the different data quality. The averaged $g^{(2)}$ functions are shown in Fig. 4. For each telescope combination, there is a $g^{(2)}$ function for channel A shown in blue and for channel B in purple. A Gaussian function is fitted to each signal peak, implied by the black dashed line. The correlation signal is always located at $\tau \sim 0$, so fixing the mean of the Gaussian function is not necessary. The amplitudes of the $g^{(2)}$ functions for both colours for the telescope combination 1–3 are smaller than for the other combinations due to 1–3 having the largest projected baselines during the measurements. The channel B data (375 nm, purple) always show smaller amplitudes than the channel A data (470 nm, blue). There are two reasons for this: the coherence time $\tau_c \approx \lambda_0^2/(c\Delta\lambda)$ is smaller for light at smaller wavelengths, and the squared visibility curves for smaller wavelengths decrease more

[6]See https://spectrum-instrumentation.com/products/details/M4i2211-x8.php.
[7]See https://adnacom.com/r34/.

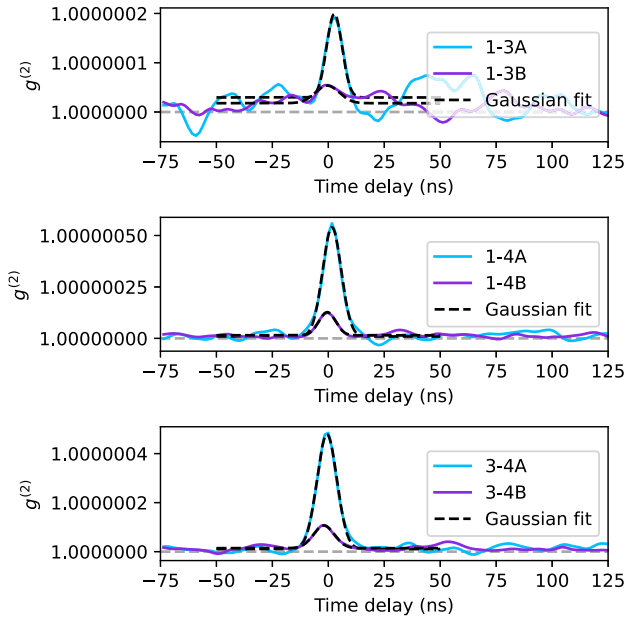


**Figure 4.** The $g^{(2)}$ functions of the accumulated data of all stars for each telescope combination. The upper plot shows telescope combination 1–3, the middle plot 1–4, and the lower plot 3–4. The blue curve represents the $g^{(2)}$ function of the measurements of channel A with the 470-nm interference filter and the purple curve the measurements of channel B with the 375-nm filter. The black dashed line is the Gaussian fit (including vertical offset) to each data curve.

**Table 1.** List of the measurement segments and segment times in minutes for each star.

| Night (mm/dd) | $\beta$ Cru | $\eta$ Cen | $\sigma$ Sgr | $\delta$ Sco |
|---|---|---|---|---|
| 04/27 | 4 × 24.13 | – | – | – |
| 04/28 | 8 × 22.20 | – | – | – |
| 04/29 | 3 × 25.40 | – | – | – |
| 05/03 | 6 × 24.67 | – | – | – |
| 05/04 | 9 × 27.27 | – | – | – |
| 05/06 | – | – | 8 × 40.00 | – |
| 05/07 | – | 14 × 41.74 | – | – |
| 05/08 | – | 8 × 45.40 | – | – |
| 05/09 | – | – | – | 6 × 37.27 |
| 05/10 | – | – | 3 × 40.80 | 6 × 34.93 |
| **Total** | 12.4 h | 15.79 h | 7.37 h | 7.22 h |

rapidly with increasing baselines (see equation 4), which means taking an average squared visibility over a range of baselines results in smaller values for smaller wavelengths.

For each combination and channel, the width of the Gaussian (sigma) is extracted (see Fig. 4). To receive a global sigma for each channel, the weighted average of the sigma value of the telescope combinations is calculated. We determine a global sigma of 4.33 ns for channel A and 4.06 ns for channel B.

### 5.3 Squared visibility curves

For accurate analysis of the change in squared visibility, the data of each star are divided into time segments. The length of these segments depends on the brightness of the star and the acquisition time. The details are described in Zmija et al. (2023). Table 1 shows an overview of the segments and measurement times of each star. As the star moves on its trajectory during the night, the projected

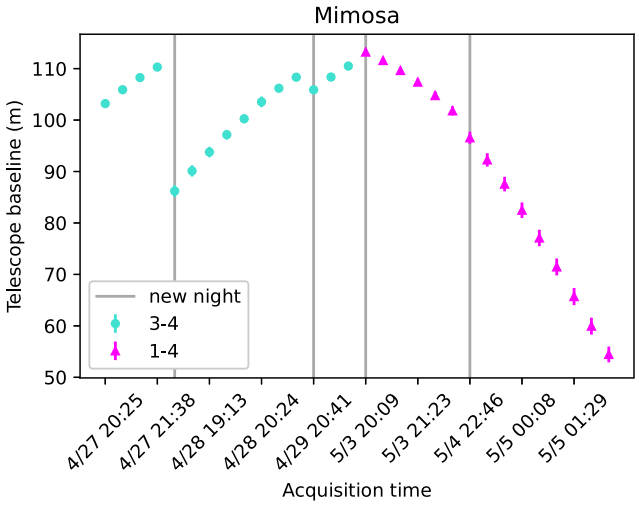


**Figure 5.** Telescope baselines for each measurement segment of the star $\beta$ Cru. The vertical lines indicate a new measurement night. The different colours represent the telescope combinations with which the measurement was taken. This plot shows the change of the projected baseline over the whole measurement period of $\beta$ Cru.

baseline changes. This is shown in Fig. 5 where the projected baseline is plotted against the acquisition time of each segment over the complete measurement time of $\beta$ Cru. The corresponding baseline for each time segment is derived by taking the average of the baselines of each data file in one segment. The errorbars imply the range of baselines within one measurement segment and are the $1\sigma$ distribution. The cyan points represent measurements taken with telescope combination 3–4 and the pink points with telescope combination 1–4. The vertical grey lines indicate a new observation night.

To extract the squared visibility, a Gaussian is fitted to the $g^{(2)}$ function of each segment. In order to prevent fitting into fluctuations, we fix the Gaussian width sigma, which is quite stable. Thus, we only fit the mean and the amplitude of the Gaussian. The integral of the fitted Gaussian is plotted against the projected baseline, as seen in Fig. 6 for each colour separately. Again, the cyan points represent measurements taken with telescope combination 3–4 and the pink points with telescope combination 1–4. In order to properly consider the effects of the stochastic photon noise on the uncertainty, we derive the errors of the integral with the following approach. The photon bunching peak, modelled as a Gaussian, is extracted by a fit into the data, and then added on to 160 independent intervals of the $g^{(2)}$ function left and right of the actual peak, which usually consist of different realizations of stochastic noise only. In each interval, the peak is re-fitted and its integral computed. The $1\,\sigma$ distribution of the reconstructed integrals is considered the uncertainty on the measurement.

### 5.4 Angular diameter analysis

To analyse the angular diameter of our targets, we take both the uniform disc (UD) and the limb darkening (LD) model into account. In the case of the UD model (see equation 4), we use the following fit function:

$$f(b) = A|g^{(1)}(b)|^2 = A\left[\frac{2J_1(\pi b\theta_{\mathrm{UD}}/\lambda)}{\pi b\theta_{\mathrm{UD}}/\lambda}\right]^2, \tag{6}$$

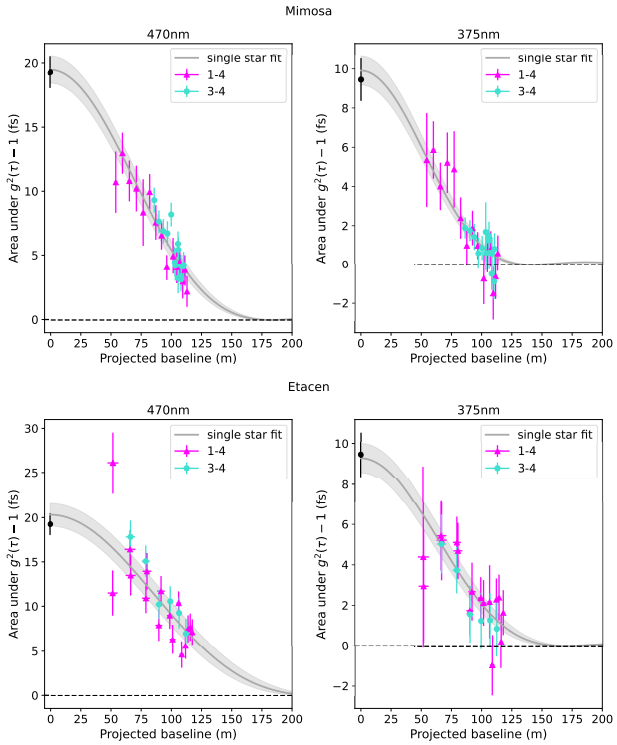


**Figure 6.** Obtained squared visibility as a function of the projected baseline (m). The upper and lower panels show the spatial coherence of $\beta$ Cru and $\eta$ Cen, respectively. The left and right panels show the 470- and 375-nm filters, respectively. The data points resulting from different telescope combinations are presented in different colours. The black data point displays the spatial coherence value at the zero baseline. The grey curve represents the fit of the LD model and is referred to as the single-star fit.

**Table 2.** Zero baseline amplitudes computed by the UD fit model (in fs) for each filter colour and their weighted average.

| Filter | $\beta$ Cru | $\eta$ Cen | $\sigma$ Sgr | Weighted average |
|---|---|---|---|---|
| 470 nm | $19.80 \pm 1.86$ | $22.68 \pm 2.44$ | $15.89 \pm 2.13$ | $19.23 \pm 1.22$ |
| 375 nm | $12.06 \pm 1.89$ | $8.60 \pm 1.51$ | $6.61 \pm 2.83$ | $9.45 \pm 1.09$ |

where $b$ is the projected baseline, and $\lambda$ is the central wavelength of the interference filter (either 470 or 375 nm). For fitting, we use the orthogonal distance regression (odr) algorithm from SCIPY, which takes both vertical and horizontal errorbars into account. From the fit, we gather the angular diameter $\theta_{\rm UD}$ and the 'zero baseline amplitude' $A$. The expected value of the latter, $A_{\rm expect}$, corresponds to

$$A_{\rm expect} = \int_{-\infty}^{+\infty} \left[ g^{(2)}_{\rm expect}(\tau, b=0) - 1 \right] {\rm d}\tau = 0.5 k_T \, \tau_{\rm c}, \tag{7}$$

where $\tau_c$ is defined in equation (5) and the factor $k_T$ is a calculated correction factor, which depends on the profile of the interference filters. The details are described in Zmija et al. (2023) and the results are 0.83 for the 375-nm filter and 0.84 for the 470-nm filter. As our light is unpolarized, a factor of 0.5 is added to the equation. This leads to an expected zero baseline amplitude of $A_{\rm expect} = 19.45$ fs for the 375-nm filter and $A_{\rm expect} = 31.09$ fs for the 470-nm filter, whereas the fit gives a parameter that is smaller by a factor of 2 and 1.6, respectively. Table 2 shows the fitted zero baseline amplitudes for our targets and different filter colours. One potential reason for the loss in coherence is a remaining bandwidth mismatch of the interference filters between the telescopes (see Section 3.2). An indication for this is that the loss is less severe compared to the measurements at 2 nm bandwidth in 2022. But the exact origin is still unclear and is being investigated. The correlation at zero baseline is a fixed parameter of our instruments, not depending on parameters of an observed star. Therefore, we take the zero baseline amplitudes of our investigated targets computed via the UD fit model, and estimate the weighted average for each colour. The result is also noted in Table 2. Next, we insert this value as a data point, seen, for example, in Fig. 6 as black data point at $b = 0$, and refit the UD model to all data. The resulting angular diameter of the second fit is the main outcome we document for each star and colour.

As mentioned above, we also account for LD by applying the following equation introduced by Hanbury Brown (1974):

$$f(b) = A \left( \frac{1-u_\lambda}{2} + \frac{u_\lambda}{3} \right)^{-2} \times \left[ (1-u_\lambda) \frac{J_1(x_{\rm LD})}{x_{\rm LD}} + u_\lambda \sqrt{\frac{\pi}{2}} \frac{J_{3/2}(x_{\rm LD})}{(x_{\rm LD})^{3/2}} \right]^2, \tag{8}$$

where $u_\lambda$ is the LD coefficient, $x_{\rm LD} = \pi b \theta_{\rm LD}/\lambda$, and $\theta_{\rm LD}$ is the LD angular diameter. The interpolation of the LD coefficient $u_\lambda$ is carried out as described in Abeysekara et al. (2020) with look-up tables from Claret & Bloemen (2011).

## 6 RESULTS

In this section, we summarize the results of our measurement campaign in 2023. During our observation period, data were taken of four stars in the Southern hemisphere. Both $\beta$ Crux and $\eta$ Cen are single stars and were chosen as they were also investigated by HBT, which makes them good candidates for comparison. $\sigma$ Sgr is the third single star that was observed in 2023. We studied $\sigma$ Sgr in 2022 (Zmija et al. 2023) and we compare those results in Section 6.2. The last star on our target list was $\delta$ Sco, a spectroscopic binary. We will not present a binary analysis in this paper but use a single-star model to fit to the data, which is clarified in the next section. $\delta$ Sco was also observed by HBT and treated as a single star (Hanbury Brown et al. 1974).

### 6.1 Stellar diameter results

We present the angular diameters of our measurements in 2023 April/May. All important parameters that are necessary to compute the diameter, and are mentioned in Section 5, are listed in Table 3. The table also includes the spectral type of the targets and the reference diameter. The final angular diameters for UD and LD models of our targets are presented in Table 4. The squared visibility curves are shown in Figs 6 and 7. The grey curve represents the LD model, which is referred to as the single-star fit. As can be seen in Table 4, the UD model underestimates the angular diameter compared with the LD model by $\approx 3$ per cent. If LD is corrected for properly, the LD angular diameter of one star should be the same at different wavelengths, which is not the case in our particular situation. Whilst the $\theta_{\rm UD}$ results for $\beta$ Cru and $\eta$ Cen for both colours are consistent within uncertainties, the results for $\sigma$ Sgr and $\delta$ Sco are significantly different beyond their error. The cause of these discrepancies is yet clear. They may point either to additional systematic uncertainties, which we have not considered, or to a more complex star model (rapid rotator, gravity darkening), where the stars' physical sizes differentiate at different wavelengths. As for $\sigma$ Sgr, which is indeed

**Table 3.** Stellar targets and their characteristic parameters. Spectral types and $B$ magnitudes are taken from SIMBAD. The reference angular diameters are recovered from NSII (Hanbury Brown 1974), where the stars were measured at a wavelength of 443 nm, and from Underhill et al. (1979a). $T_{\rm eff}$ is the effective temperature of the star and $\log(g)$ is the surface gravity. These are parameters needed to derive the LD coefficient $u_\lambda$.

| Name | Spectral type | $B$ (mag) | Reference $\theta_{\rm UD}$ (mas) | Source | $T_{\rm eff}$ (K) | $\log(g)$ (cm s$^{-2}$) | $u_\lambda$ |
|---|---|---|---|---|---|---|---|
| $\beta$ Cru | B1IV | 1.02 | $0.702 \pm 0.022$ | NSII | $27\,000 \pm 1000^a$ | $3.6 \pm 0.1^a$ | 0.37 |
| $\eta$ Cen | B2Ve | 2.12 | $0.47 \pm 0.03$ | NSII | $21\,000^b$ | $3.95^b$ | 0.371 |
| $\sigma$ Sgr | B2.5V | 1.923 | 0.68 | Underhill | $18\,987^c$ | $4.0^c$ | 0.385 |
| $\delta$ Sco | B0.3IV | 2.20 | $0.45 \pm 0.04$ | NSII | $30\,900 \pm 309^d$ | $3.50 \pm 0.04^d$ | 0.373 |

[a] Values are from Cohen et al. (2008). [b] Values are from Arcos et al. (2018a). [c] Values are from Underhill et al. (1979b). [d] Values are from Arcos et al. (2018b).

**Table 4.** Table of observed stars and their measured angular diameters listed with their uncertainties for the UD and LD models and for 470 and 375 nm.

| Name | 375 nm | | 470 nm | |
|---|---|---|---|---|
| | Measured $\theta_{\rm UD}$ | Measured $\theta_{\rm LD}$ | Measured $\theta_{\rm UD}$ | Measured $\theta_{\rm LD}$ |
| $\beta$ Cru | $0.676 \pm 0.017$ | $0.699 \pm 0.018$ | $0.654 \pm 0.016$ | $0.675 \pm 0.016$ |
| $\eta$ Cen | $0.56 \pm 0.02$ | $0.58 \pm 0.02$ | $0.53 \pm 0.03$ | $0.55 \pm 0.03$ |
| $\sigma$ Sgr | $0.51 \pm 0.03$ | $0.53 \pm 0.04$ | $0.61 \pm 0.02$ | $0.63 \pm 0.02$ |
| $\delta$ Sco | $0.59 \pm 0.02$ | $0.61 \pm 0.02$ | $0.66 \pm 0.01$ | $0.68 \pm 0.01$ |

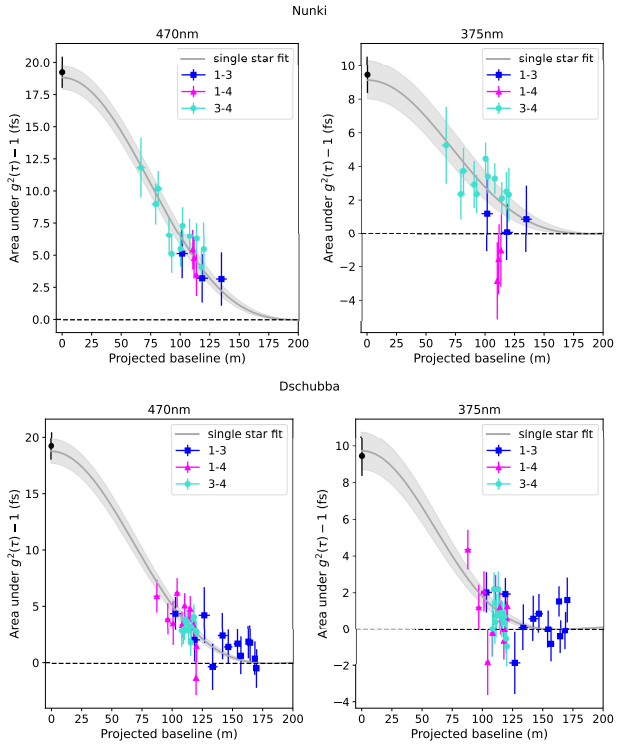


**Figure 7.** Obtained squared visibility as a function of the projected baseline (m). The upper and lower panels show the spatial coherence of $\sigma$ Sgr and $\delta$ Sco, respectively. The left and right panels show the 470- and 375-nm filters, respectively. The data points resulting from different telescope combinations are presented in different colours. The black data point displays the spatial coherence value at the zero baseline. The grey curve represents the fit of the LD model and is referred to as the single-star fit.

a rapid rotator (Abt, Levato & Grosso 2002), the reference value of 0.68 mas was measured at infrared wavelength, which would be consistent with the assumption that the star is measured larger at larger wavelengths.

For analysing $\delta$ Sco, it is important to know its binary characteristics. The two components of the spectroscopic binary are separated by 0.2 arcsec and have a magnitude of 2.2 and 4.6 (Mason et al. 2001). The system has an orbital period of 10.5 yr and the orbit is elliptical (Miroshnichenko et al. 2013). The two stars in the binary are too far apart to be resolved by the H.E.S.S. telescopes. A wobbling in the $g^{(2)}$ function caused by the separation of the two stars is expected of the order of $< 1$ m, which is averaged out by the dish diameter of the single telescopes (Rai, Basak & Saha 2021). Furthermore, the difference in magnitude indicates that the secondary has less intensity by a factor of 10. Because of these properties, we decided to present the data with a single-star fit, as shown in Fig. 7, and interpret the resulting angular diameter as the diameter of the primary. The reduced $\chi^2$ for the single-star fit for both colours is 0.92, which is consistent with the single-star model.

### 6.2 Data comparison $\sigma$ Sgr

Here we compare the results for the star $\sigma$ Sgr, where the reference angular diameter is 0.68 mas (Underhill et al. 1979a). Our first measurements from 2022 April resulted in a diameter of $0.52 \pm 0.07$ mas (Zmija et al. 2023). The optics consisted of an interference filter with 465nm CWL and 2 nm width. Further differences in our optical set-up to the measurement campaign 2023 can be found in Section 3. The angular diameter of the UD model, which we determined from the measurements of 2023, is $0.61 \pm 0.02$ mas for the interference filter with 470 nm CWL and 10 nm width. For comparison with the data of 2022, we only take a closer look at the 470 nm filter because the CWL are comparable. Fig. 8 shows the normalized squared visibility curves of both campaigns. Another aspect, which has to be mentioned, is the observation time of the star. In 2022, measurements of $\sigma$ Sgr were taken for 11:59 h, whereas in 2023 it was only 7:25 h. The results are consistent within 1.2 standard deviations, where the uncertainty in 2023 was strongly reduced compared with 2022, despite less observation time. The reasons are the (partial) simultaneous operation of three telescopes instead of only two (which results in three simultaneous measurements instead of only one), and the more precise determination of the zero baseline amplitude.

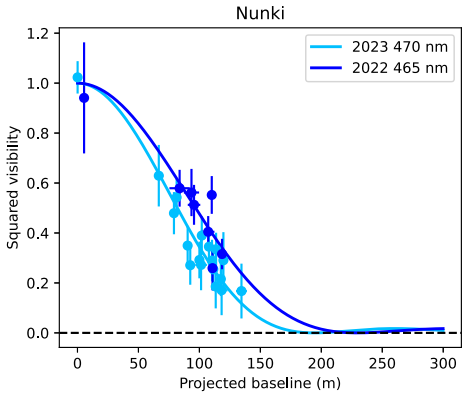


**Figure 8.** Squared visibility of $\sigma$ Sgr is shown as a function of the projected baseline (m). The light blue data represent the results of the 2023 campaign and the dark blue data the 2022 campaign. The data were normalized to one to make the visual comparison easier.

## 7 CONCLUSION AND OUTLOOK

In this paper, we have presented our results of the 2023 intensity interferometry campaign at the H.E.S.S. telescopes. Our two campaigns of 2022 and 2023 demonstrate how well IACTs are suited for intensity interferometry during full Moon periods, when they are not able to perform gamma-ray observations.

Several goals for updating our set-up were met. To gain more telescope baselines, three telescopes were equipped with our set-up. The bandwidth of the interference filters was increased from 2 to 10 nm and the set-up was updated to measure in two colours (375 and 470 nm) simultaneously. We measured the diameters of four stars, not only with the UD model but also taking the LD model into account. The precision of the extracted diameters is at a level of a few per cent within a reasonable measurement time. The results for $\beta$ Cru and $\eta$ Cen between the two colours are consistent within uncertainties. Comparing the resulting angular diameters of $\sigma$ Sgr, they become smaller with shorter wavelengths, which is the same case for the results of $\delta$ Sco. This effect might be attributed to a more intricate stellar model. H.E.S.S. is the first IACT to perform intensity interferometry with two colours simultaneously. This marks substantial progress towards implementing intensity interferometry with the CTAO, as this approach might eventually set the standard for these measurements and promises enhancements in signal-to-noise ratio.

In the future, all four H.E.S.S. Phase I telescopes will be equipped with an intensity interferometry set-up to supply a broad coverage in the two-dimensional baseline map ('uv plane'). Furthermore, the mechanical and computational set-up will be updated in order to be able to execute observations remotely. A method to restrict the value of the zero baseline amplitude would be to have a calibration source or star, which produces strong correlation signals due to its brightness and covers a large baseline range for good restriction with the fit model. This is done by MAGIC and described in Abe et al. (2024). For the H.E.S.S. telescopes, the ideal target would be the star $\beta$ Cru. Future targets will involve fainter single stars to determine the sensitivity of our system. Not only single stars in the Southern hemisphere will be observed but also binary star systems with various characteristics.

## ACKNOWLEDGEMENTS

We thank the H.E.S.S. Collaboration for reviewing this work and for allowing us to use their telescopes for our measurement campaign. We also thank the H.E.S.S. local crew for their support on site and the operations team for their help online. This work was supported with a grant by the Deutsche Forschungsgemeinschaft ('Optical intensity interferometry with the H.E.S.S. gamma-ray telescopes', FU 1093/3-1).

## DATA AVAILABILITY

The data underlying this article will be shared on reasonable request to the corresponding author. Correlation histograms are available in time intervals of 3.436 s. Due to the large size of the digitized waveforms in excess of several TB, the raw data cannot be made available online.

## REFERENCES

Abe S. et al., 2024, MNRAS, 529, 4387
Abeysekara A. et al., 2020, Nature Astron., 4, 1164
Abt H. A., Levato H., Grosso M., 2002, ApJ, 573, 359
Acciari V. et al., 2020, MNRAS, 491, 1540
Acharyya A. et al., 2024, ApJ, 966, 28
Arcos C., Kanaan S., Chávez J., Vanzi L., Araya I., Curé M., 2018a, MNRAS, 474, 5287
Arcos C., Kanaan S., Chávez J., Vanzi L., Araya I., Curé M., 2018b, MNRAS, 474, 5287
Claret A., Bloemen S., 2011, A&A, 529, A75
Cohen D. H., Kuhn M. A., Gagné M., Jensen E. L. N., Miller N. A., 2008, MNRAS, 386, 1855
Cortina J. et al., 2022, Proc. SPIE, 12183, 121830C
Dravins D., 2016, Proc. SPIE, 9907, 99070M
Dravins D., LeBohec S., Jensen H., nez P. D. N., 2013, Astropart. Phys., 43, 331, https://doi.org/10.1016/j.astropartphys.2012.04.017
Ferreira D., Bachelard R., Guerin W., Kaiser R., Fouché M., 2020, American Journal of Physics, 88, 831
Haguenauer P. et al., 2010, Proc. SPIE, 7734, 773404
Hanbury Brown R., 1974, The Intensity Interferometer: Its Application to Astronomy. Halsted, New York
Hanbury Brown R., Davis J., Allen L. R., 1967, MNRAS, 137, 375
Hanbury Brown R., Davis J., Allen L. R., 1974, MNRAS, 167, 121
Kieda D. B., 2022, Proc. SPIE, 12183, 121830D
LeBohec S., Holder J., 2006, ApJ, 649, 399
Mandel L., Wolf E., 1995, Optical Coherence and Quantum Optics. Cambridge Univ. Press, Cambridge
Mason B. D., Wycoff G. L., Hartkopf W. I., Douglass G. G., Worley C. E., 2001, AJ, 122, 3466
Miroshnichenko A. S. et al., 2013, ApJ, 766, 119
Rai K. N., Basak S., Saha P., 2021, MNRAS, 507, 2813
Siegert A. J. F., 1943, On the Fluctuations in Signals Returned by Many Independently Moving Scatterers. Radiation Laboratory, Massachusetts Institute of Technology, Cambridge, MA
ten Brummelaar T. A. et al., 2005, ApJ, 628, 453
Underhill A. B., Divan L., Prévot-Burnichon M.-L., Doazan V., 1979b, MNRAS, 189, 601
Underhill A., Divan L., Prevot-Burnichon M.-L., Doazan V., 1979a, MNRAS, 189, 601
Zmija A., Vogel N., Anton G., Malyshev D., Michel T., Zink A., Funk S., 2021, MNRAS, 509, 3113
Zmija A., Vogel N., Wohlleben F., Anton G., Zink A., Funk S., 2023, MNRAS, 527, 12243

This paper has been typeset from a TEX/LATEX file prepared by the author.